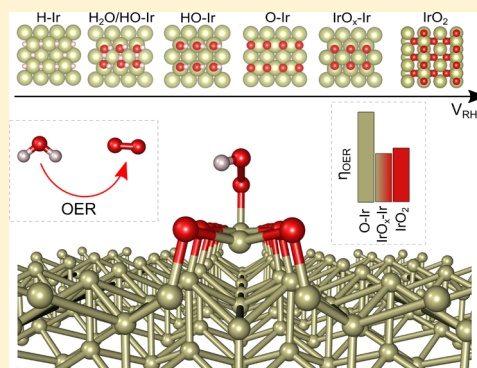


Ab Initio Thermodynamics of Iridium Surface Oxidation and Oxygen Evolution Reaction

Konstantin Klyukin,[†] Alexandra Zagalskaya,[†] and Vitaly Alexandrov^{*,†,‡,§}[†]Department of Chemical and Biomolecular Engineering and [‡]Nebraska Center for Materials and Nanoscience, University of Nebraska—Lincoln, Lincoln, Nebraska 68588, United States

ABSTRACT: Iridium-based materials are considered as state-of-the-art electrocatalysts for oxygen evolution reaction (OER), however, their stability and catalytic activity greatly depend on surface-state changes induced by electrochemical cycling. To better understand the behavior of the low-index Ir surfaces in an electrochemical environment, we perform a systematic thermodynamic analysis by means of the density functional theory (DFT) calculations. On the basis of computed surface energies of the Ir (111), (110) and (100) facets as a function of applied electrode potential and coverage of adsorbed water species we determine stability maps and predict equilibrium shapes of Ir nanoparticles. Our calculations also show that metastable oxide precursors formed at the initial stages of Ir surface oxidation are responsible for enhanced catalytic activity toward OER as compared to metal surfaces covered by oxygen adsorbates and thick-oxide films. Such enhancement occurs not only due to the modified thermodynamic stability of OER intermediates, but also because thin-oxide layers may display the more energetically favorable I2M (interaction of two M–O units) rather than WNA (water nucleophilic attack) OER mechanism.



INTRODUCTION

Iridium is considered as one of the best catalysts toward oxygen evolution reaction (OER) because of the favorable combination of properties including high corrosion resistance and the low overpotential (ca. 0.3 V) required for the reaction to proceed.^{1,2} Ir-based materials have also been used as electrodes for a variety of other catalytic processes including hydrogen oxidation^{3,4} and evolution,^{4,5} oxidation of carbon monoxide⁶ and ethanol.⁷ Despite good catalytic activity, corrosion stability of Ir electrodes is an issue and a number of recent investigations were directed at understanding their activity-stability relationships.^{8–10} It is now recognized that electrocatalytic activity for OER and electrode corrosion are linked across a variety of noble metals including Ir,^{7,11,12} however, questions about the underlying atomistic mechanisms and to what extent these two processes are correlated remain open.¹³

Corrosion of noble metal electrodes is a complicated phenomenon comprised of a series of coupled chemical processes such as surface oxidation and formation of defects, facet-dependent dissolution and deposition processes.¹⁴ In electrochemical environments, adsorbed water species formed at different potentials can preferentially stabilize specific facets and induce surface restructuring due to significant anisotropic changes in surface energies.¹⁵ One of the key experimental findings about the relationship between activity and stability of Ir electrodes is the identification of transient surface states characterized by the formation of nonstoichiometric IrO_x species that lead to an enhanced OER performance.¹⁶ Once the surface is transformed to thermodynamically stable IrO₂,

the stability is increased, while activity is decreased. This in part explains why electrochemically treated Ir electrodes exhibit higher electrocatalytic activity for OER than thermally prepared rutile-type IrO₂ systems,^{10,17} which appears to be common across noble metals.¹⁸ The formation of surface oxide layers on Ir was shown to occur before the onset of OER and metal–oxide species with different Ir oxidation states may coexist during OER.^{1,10,19} Unlike extensive computational research on Pt, atomistic modeling studies of Ir in aqueous environments are still very limited.^{20–22} Experimental investigations, however, demonstrate that significant differences in electrochemical behavior of the two noble metals can be observed. For example, Ir exhibits higher OER activity than Pt, but it also corrodes faster. While previous experimental studies have provided some microscopic insights into the changes in surface structure and chemistry induced by OER, more atomistic information is required to better understand the complex interplay between activity, stability and evolution of the Ir surfaces in electrochemical environments. In this paper we employ *ab initio* thermodynamics approach to analyze stability of (111), (110) and (100) surfaces of Ir in aqueous solutions as a function of electrode potential and shed some light on the role of Ir–oxide precursors formed on Ir in facilitating OER.

Received: October 9, 2018

Revised: November 22, 2018

Published: December 3, 2018

■ COMPUTATIONAL METHODOLOGY

All DFT calculations were performed using the generalized gradient approximation Perdew–Burke–Ernzerhof (PBE) exchange–correlation functional²³ as implemented in Vienna ab initio simulation package (VASP).^{24,25} The PBE functional was corrected for long-range dispersion interactions using the D3 approach according to Grimme formalism.^{26,27} A cutoff energy of 450 eV was used, and the convergence criteria for the energy and forces were 10^{-6} eV and 0.02 eV/Å during structural optimization, respectively. The Ir *fcc* bulk structure with a lattice constant of 3.87 Å was used to generate Ir(111), Ir(100), and Ir(110) four-layer slabs separated by a vacuum gap of 15 Å. The bottom two layers of the slabs were fixed while the top two layers were allowed to relax. The 3×3 surface cells with a $5 \times 5 \times 1$ Monkhorst–Pack mesh to sample the *k*-space were employed for all surfaces. Dipole correction²⁸ was used in the surface normal direction (using keywords LDIPOL = TRUE, IDIPOL = 3). The adsorption of water dissociation products (O, OH, H) was considered at the *top*, *bridge*, *fcc* and *hcp* surface sites. To determine the most energetically favorable adsorption sites we used the Gibbs free energies of hydrogen and oxygen adsorption reactions defined as

$$\Delta G_{\text{H}}^{\text{ads}} = G_{\text{H}^*} - G_{*} - G_{\text{H}_{\text{aq}}^{+}} \quad (1)$$

$$\Delta G_{\text{O}}^{\text{ads}} = G_{\text{O}^*} - G_{*} - G_{\text{H}_2\text{O}_{(\text{aq})}} + 2G_{\text{H}_{\text{aq}}^{+}} \quad (2)$$

where G_{H^*} and G_{O^*} are the free energies of the surface with adsorbates (hydrogen and oxygen, respectively), G_{*} is the energy of the bare surface, $G_{\text{H}_2\text{O}_{(\text{aq})}}$ and $G_{\text{H}_{\text{aq}}^{+}}$ are the free energies of the solution phase water and proton. The free energy of the surface with an adsorbate was computed as

$$G = E^{\text{tot}} + ZPE - TS_{\text{vib}} \quad (3)$$

where E^{tot} is the total energy, ZPE is the zero-point energy, S_{vib} - vibrational entropy, T is temperature taken as 300 K in all calculations. The free energies of aqueous hydrogen $G_{\text{H}_{\text{aq}}^{+}}$ and water $G_{\text{H}_2\text{O}_{(\text{aq})}}$ were calculated at 0.035 bar and 300 K. Zero-point energies and vibrational entropies were estimated by computing the vibrational spectra based on the finite differences method (IBRION = 5).

Constrained *ab initio* thermodynamics approach was applied to study the most stable electrode surface structure as a function of the potential assuming that the actual reaction on the electrocatalyst surface is suppressed.^{29,30} The surface energy $\gamma(U)$ was calculated as a function of potential as described in ref 31

$$\gamma(U) = \gamma_{\text{bare}} + \frac{G_{\text{H}^*} - G_{*} - G_{\text{H}_{\text{aq}}^{+}} + eU}{A} \quad (4)$$

$$\gamma(U) = \gamma_{\text{bare}} + \frac{G_{\text{OH}^*} - G_{*} - G_{\text{H}_2\text{O}_{(\text{aq})}} + (2-x)G_{\text{H}_{\text{aq}}^{+}} - (2-x)eU}{A} \quad (5)$$

where γ_{bare} is the surface energy of the bare surface, G_{H^*} and G_{OH^*} are the free energies of the surface with adsorbed water products (x can be 0 or 1 to represent O^* or OH^* adsorption), U is the applied potential, e is the electron charge, and A is the

surface area of iridium. The electrode potential is parametrized within the computational hydrogen electrode scheme³² and the free energy of the aqueous phase proton, $G_{\text{H}_{\text{aq}}^{+}}$, is linked to the pH-independent reversible hydrogen electrode V_{RHE} . The Wulffmaker package³³ was used to predict equilibrium crystal geometries of Ir nanoparticles based on the calculated surface energies. We note that our analysis is limited to the low-index facets of Ir, however, high-index surfaces (kinks, steps, edges) should also contribute to nanoparticle faceting and affect the overall catalytic activity of Ir nanoparticles.³⁴

To compute the thermodynamic overpotential (also known as the Gibbs energy loss^{29,30,35}) of OER, we chose to employ the revised PBE (RPBE) exchange–correlation functional to be consistent with previous computational investigations.^{36,37} Although thermodynamic overpotentials for OER were found to be sensitive to the choice of an exchange–correlation functional³⁸ and could be affected by explicit treatment of water environment,³⁹ our tests for Ir(111) surface have shown that surface free energy plots are qualitatively similar for PBE, RPBE and PW91 functionals, while the absolute potentials could vary in the range of $\pm 0.05 V_{\text{RHE}}$.

■ RESULTS AND DISCUSSION

We start by determining the most energetically favorable adsorption sites through calculation of the Gibbs free energies of water dissociation products (O^* , H^* , and OH^*) at different surface coverages for the Ir(111), Ir(100), and Ir(110) facets. Next, we construct surface free energy plots as a function of reversible hydrogen electrode potential (V_{RHE}) and determine nanoparticle faceting under the applied potential through the Wulff constructions. We then analyze thermodynamic stability of Ir oxide layers formed at high electrode potentials and catalytic activity of Ir surfaces toward OER. The obtained computational results are also discussed in the context of available experimental data.

Identifying Thermodynamically Most Stable Adsorbate Structures on Ir Surfaces as a Function of Applied Electrode Potential. Our analysis of the interaction energetics for the aqueous species adsorbed at the low-index Ir surfaces under $V_{\text{RHE}} = 0$ shows that adsorption energies generally follow the trends common to *fcc* metals,⁴⁰ although some specific features are also observed for Ir. We first analyze adsorption properties of the Ir(111) surface which has the lowest surface energy of 2.26 J/m² under ultrahigh vacuum (UHV) conditions. Calculations show that at the lowest coverage attainable for the 3×3 surface cell (1/9 ML) hydrogen has $\Delta G_{\text{H}}^{\text{ads}}$ of -0.24 , -0.17 , -0.19 , and -0.22 eV/atom for *fcc*, *top*, *bridge*, and *hcp* sites, correspondingly. At 1 ML coverage of hydrogen, *top* sites become slightly more favorable with $\Delta G_{\text{H}}^{\text{ads}}$ of -0.23 eV/atom; however, due to small differences in energies across the surface sites, the traces of H at *top*, *fcc*, and *hcp* sites could be detected in experiments.⁴¹ These results are in qualitative agreement with the results obtained for hydrogen adsorption on the Pt(111) facet where *fcc* sites were found to be most energetically favorable,³¹ but the energy difference between various sites turns out to be negligible.⁴² We find that atomic oxygen prefers to occupy *fcc* hollow sites on Ir(111) for all considered coverages with $G_{\text{O}}^{\text{ads}}$ of 0.66 eV/atom at the coverage of 1/9 ML that becomes considerably larger (1.41 eV/atom) for the fully covered Ir(111) surface, in agreement with previous theoretical results.²⁰

The Ir(110) and Ir(100) surfaces are determined to be less stable than Ir(111) with the estimated surface energies of 2.81 and 2.83 J/m², respectively, and expectedly exhibit stronger adsorption for both H and O due to the lower coordination of surface Ir atoms. On both surfaces H atom adsorbs preferentially at the bridging sites for all the coverages in accordance with recent experiments for Ir(100).⁴³ The Gibbs free energies of H adsorption ($\Delta G_{\text{H}}^{\text{ads}}$) are estimated at -0.53 eV/atom and -0.39 eV/atom for 1 ML coverage on Ir(100) and Ir(110), correspondingly. A higher affinity of these surfaces for H adsorption results in adsorption of H even above 1 ML similar to the case for Pt.⁴⁴ In this case, hydrogen atom occupies long-bridging sites between the two Ir atoms in adjacent rows on Ir(110) and an unoccupied bridging site on Ir(100). This leads to slightly less negative $\Delta G_{\text{H}}^{\text{ads}}$ of -0.47 and -0.32 eV/atom for 1.25 ML on Ir(100) and 1.33 ML on Ir(110). In accordance with previous studies^{21,22} oxygen also prefers to occupy the bridging sites for all considered coverages on Ir(100) and Ir(110) with $\Delta G_{\text{O}}^{\text{ads}}$ of 0.76 and 0.49 eV/atom for 1 ML, correspondingly, while the adsorption of extra oxygen species beyond 1 ML is found to be highly unfavorable as opposed to H adsorption. Overall, Ir exhibits a higher propensity for surface oxidation and weaker hydrogen binding as compared to Pt,³¹ which should result in some differences in the interfacial structure of the two metals under applied potential as will be described in the next section. This is consistent with the fact that Pt serves as the state-of-the-art catalyst for hydrogen evolution reaction, while Ir-based compounds are preferred catalysts for oxygen evolution reaction. Below we use surface hydroxylation patterns recently obtained for hydroxylated Pt surfaces.^{31,45} In particular, several coadsorption configurations of OH and H₂O are considered: coadsorption of single OH with H₂O molecules, equal portion of OH and H₂O molecules, which maximizes the number of hydrogen bonds between coadsorbates, and full coverage with OH species.

Having established the most favorable adsorption configurations under $V_{\text{RHE}} = 0$, we next construct thermodynamic stability maps for the Ir surfaces with adsorbed water species as a function of relative hydrogen electrode potential (V_{RHE}). As a general feature across all the three Ir facets we observe preferential hydrogen adsorption at low potentials (starting below 0 V_{RHE}) followed by adsorption of hydroxide and water, and then by adsorption of oxygen at high potentials, in qualitative agreement with previous studies for Pt.^{31,44} The actual positions of adsorption/desorption regions, however, strongly depend on the specific Ir surface and the surface coverage revealing a few important differences between Ir and Pt as alluded to below.

Figure 1 shows the computed stability map for the Ir(111) surface. It is seen that hydrogen adsorbs at potentials below 0.15 V_{RHE} followed by an adsorption mode of coadsorbed OH* and H₂O* which is thermodynamically favorable up to about 0.8 V_{RHE} . The found overlap between H* and OH* adsorption regions for Ir(111) was not observed in the case of Pt(111) for which the two adsorption regions are separated by a ~ 0.3 V_{RHE} region where bare Pt(111) is more stable.⁴⁴ This result compares well with experimental data on Ir where hydrogen stripping/adsorption was detected in the range of 0.05–0.30 V_{RHE} .^{7,46} Also, although some of the previous experimental studies assumed that H* and OH* adsorption regions can be separated by a wide double-layer region similarly to Pt,^{47,48} several more recent investigations

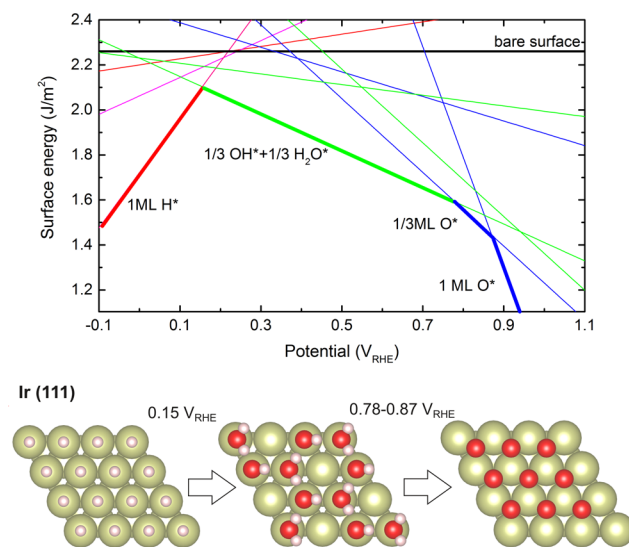


Figure 1. Surface energy as a function of potential and O/OH/H coverage on the Ir(111) surface. Bold lines define the most stable configuration under considered potential. Red, green and blue lines correspond to various H, OH+H₂O and O coverages, respectively. The bottom panel represents structural changes on the Ir(111) surface.

suggested that OH* adsorption should occur at ~ 0.25 – 0.35 V_{RHE} .^{3,7,19,49} The coadsorption of H* and OH* is also supported by a low dissociation barrier for H₂O on the Ir(111) surface that is not the case for Pt(111).⁵⁰ The overlap between H* and OH* adsorption regions along with a weak binding of H on Ir(111)⁵¹ could also help explain superior activity of Ir(111) toward hydrogen oxidation reaction.³ Regarding the oxygen binding we find that this becomes favorable at potentials beyond 0.8 V_{RHE} , in good agreement with experimental studies where the peak corresponding to the oxygen adsorption/desorption on Ir(111) was observed at about 0.9 V_{RHE} .^{7,49}

Under applied potential, Ir(100) and Ir(110) exhibit stronger binding of water species than Ir(111) exactly as in the case of $V_{\text{RHE}} = 0$. While for Ir(110) the hydrogen desorption peak does not shift significantly because of the competition for adsorption with OH*, hydrogen desorption at Ir(100) starts at 0.16 V_{RHE} higher potential than it is found for Ir(111) (see Figures 1–3). Experimentally measured voltammograms for the Ir(100) surface⁴⁶ feature two different peaks in the hydrogen adsorption region which could be explained by adsorption/desorption of an extra H layer (1.25 ML), while the peak at a more positive potential corresponds to strongly adsorbed H* at 1 ML coverage. The shoulder observed in the Ir(110) voltammogram⁵² probably has a similar nature. On the other hand, the absence of this feature in the case of Ir(111) can be explained by a much weaker hydrogen adsorption precluding the formation of a second H* layer at considered potentials.

Similar Ir(111), H* and OH* adsorption regions are found to overlap for both (110) and (100) surfaces. The OH* + H₂O* region turns out to be the narrowest for Ir(100). Oxidation of Ir(110) and Ir(100) starts at about 0.6 and 0.53 V_{RHE} , respectively, slightly below the experimentally measured oxidation potentials of around 0.7 V_{RHE} .^{46,52,53} Overall, the Ir(100) and (110) facets could be expected to be more prone to the oxide formation than Ir(111) for which oxidation starts

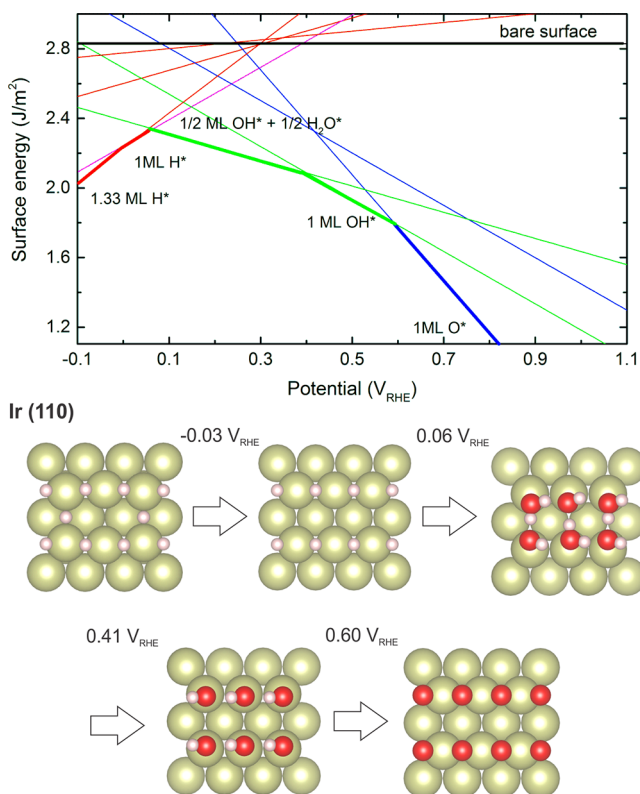


Figure 2. Surface energy as a function of potential and O/OH/H coverage on the Ir(110) surface. Bold lines define the most stable configuration under considered potential. Red, green, and blue lines correspond to various H, OH + H₂O, and O coverages, respectively. The bottom panel represents structural changes on the Ir(110) surface.

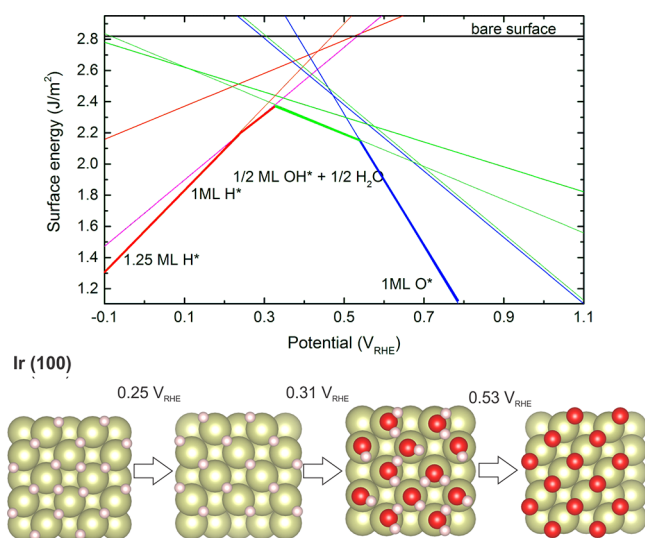


Figure 3. Surface energy as a function of potential and O/OH/H coverage on the Ir(100) surface. Bold lines define the most stable configuration under considered potential. Red, green and blue lines correspond to various H, OH + H₂O, and O coverages, respectively. The bottom panel represents structural changes on the Ir(100) surface.

at 0.78 V_{RHE}. The obtained results are in agreement with experiments where mixed OH* + H* adsorption on Ir polycrystalline nanoparticles was detected at 0.6–0.65 V_{RHE}⁵⁴

and 0.75–0.9 V_{RHE}⁷ depending on the experimental conditions. Because of higher oxophilicity, oxidation of Ir occurs at lower potentials relative to Pt,⁴⁴ where surface oxidation starts at 1.1, 0.9, and 1.2 V_{RHE} for Pt(111), Pt(100) and Pt(110), correspondingly.

Faceting of Ir Nanoparticles in Electrochemical Environments. As clearly seen from Figures 1–3, the calculated surface energy for each Ir facet with adsorbed aqueous species strongly depends on the applied electrode potential that should determine the thermodynamic driving force for surface restructuring and define equilibrium shapes of Ir nanoparticles. By using the surface energies computed above we construct the Ir nanoparticles employing the Gibbs–Wulff theorem. Figure 4 shows that under UHV conditions Ir nanoparticles should be primarily comprised of the close-packed Ir(111) facets (86%) with a small contribution of the (100) surface (14%). Under electrochemical conditions at low V_{RHE} the thermodynamic stability of the (100) surface increases due to strong hydrogen adsorption facilitating the growth of the (100) facet up to 45% at 0 V_{RHE}. At higher potentials a strong binding of hydroxyls and water to Ir(110) results in a larger contribution of this facet – 31% at 0.3 V_{RHE}. Surface oxidation increases contribution from the Ir(110) facet up to 70%. These computational results are in qualitative agreement with experimental observations of thermal faceting of Ir nanocrystals under UHV conditions where the formation of cuboctahedral Ir nanoparticles exposing only the Ir(100) and (111) facets was observed, whereas upon Ir oxidation the traces of (110) and (113) were also detected.^{55,56} The formation of these facets was also revealed upon restructuring of Ir(210) in oxygen environment.⁵⁶ Qualitatively, our results compare well with DFT-based Wulff constructions for Pt nanoparticles,⁴⁴ however, we find that Ir oxidation takes place at lower potentials reflecting a higher oxophilicity of Ir as compared to Pt.

Stability of Ir Oxide Layers. It is experimentally established that the electrocatalytic activity of noble metals is related to the formation of surface oxide layers. Moreover, the formation of transient nonstoichiometric IrO_x species on Ir surfaces during OER was determined to play a key role in stability-activity relationships of Ir.^{16,17} To better understand the stability of Ir oxide layers under electrochemical conditions as well as the surface catalytic activity we next carry out the analysis of thermodynamic stability of water species on partially oxidized Ir surfaces. It is worth noting that complete description of oxide formation and the corresponding restructuring of Ir surface should involve a kinetic analysis of both dissolution and deposition processes and is beyond the scope of this study. We also note that these processes should be kinetically hindered at low potentials, and therefore, the onset potential predicted using thermodynamic approach is expected to be underestimated relative to experimental values.

To analyze thermodynamic stability of Ir oxide thin-films in an electrochemical environment we adopt the structures of Ir oxide layers from the literature. The O–Ir–O trilayer structure (see Figure 5) is considered as an oxide precursor formed at the Ir(111) surface as suggested by previous experimental and theoretical studies.^{20,57} This structure could be formed through the extraction of Ir atoms from the surface covered by adsorbed oxygens through the buckling mechanism with a relatively small activation barrier as it was previously found for Pt.⁵⁸ Our calculations reveal that the O–Ir–O trilayer becomes thermodynamically favorable at potentials above 0.7

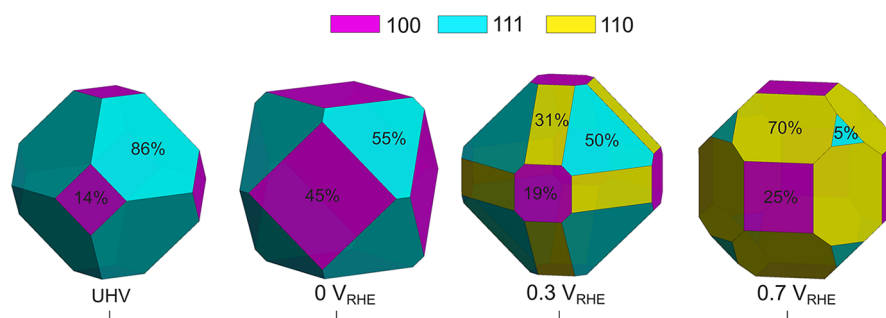


Figure 4. Equilibrium nanoparticle shapes based on Wulff constructions under UHV conditions and as a function of applied potential with the corresponding fractions of each facet.

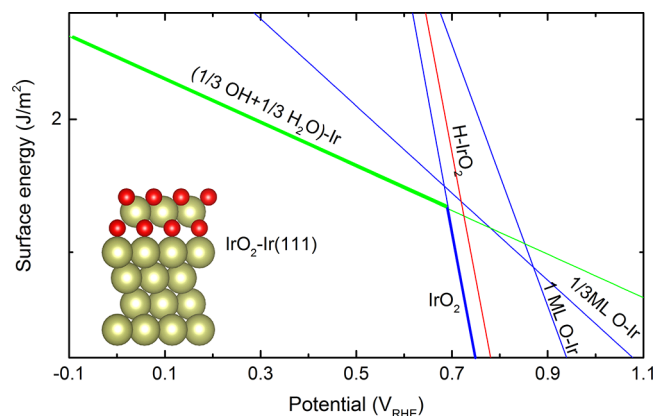


Figure 5. Surface energy as a function of potential and O/OH/H coverage on the IrO₂-Ir(111) surface. Bold lines define the most stable configuration under considered potential. Red, green, and blue lines correspond to various H, OH, and O coverages, respectively. Lines for the Ir metal surface are presented as a reference. The inset represents a structural model of the oxide precursor on the Ir(111) surface.

V_{RHE} (Figure 5). However, since the formation of surface oxides requires restructuring of the top Ir layers and diffusion of O into the subsurface, the oxide formation is kinetically limited in experiments with irreversible oxidation occurring only at high potentials ($>1-1.2 V_{\text{RHE}}$).^{1,8,52} We find that protonation of top surface oxygens is highly unfavorable at the considered potential window, unlike metallic Ir(111) (Figure 1). Therefore, the oxide layer should be more stable upon cycling at low potentials which is in agreement with experiments revealing that the oxidized Ir(111) surface does not exhibit hydrogen adsorption and desorption at low potentials.⁵²

In contrast to Ir(111), Ir(110) is experimentally known to display faster surface oxidation which was attributed to less severe structural changes and more open structure.⁵² It can be assumed that the formation of the oxide precursor on Ir(110) starts with oxygen adsorption to form IrO₂-like stripes along the Ir ridges followed by ejection of Ir atoms to the surface similarly to Pt(110).⁵⁹ In this case the formation of the Ir(110) surface oxide appears to be more energetically favorable than simple oxygen adsorption at potentials higher than ca. $0.6 V_{\text{RHE}}$ (see Figure 6). However, it requires to overcome an additional barrier associated with surface restructuring that leads to higher experimentally measured potentials of ca. $0.9 V_{\text{RHE}}$.⁵²

Since the oxidized Ir(110) surface has Ir atoms exposed to the environment, we next examine further oxidation of this surface by adsorbing O* and OH* to form intermediates that

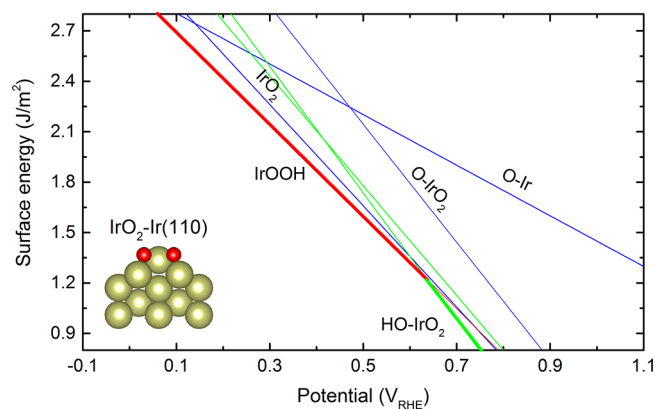


Figure 6. Surface energy as a function of potential and O/OH/H coverage on the IrO₂-Ir(110) surface. Bold lines define the most stable configuration under considered potential. Red, green, and blue lines correspond to various H, OH and O coverages, respectively. Lines for the Ir metal surface are presented as a reference. The inset represents a structural model of the oxide precursor on the Ir(110) surface.

could play an important role in both OER and dissolution processes. Specifically, we find that under high potentials ($>0.62 V_{\text{RHE}}$) the oxide is covered with hydroxyl adsorbates forming IrO₂-OH clusters on metallic Ir surface, while adsorption of OH* on the same Pt surface is found to be weak becoming favorable only at high potentials ($>1.2 V_{\text{RHE}}$). However, high concentration of OH* on the IrO₂-Ir(110) surface is determined to cause irreversible structural transformations. After cycling back to potentials lower than $0.5 V_{\text{RHE}}$ the surface oxide could be destroyed due to the protonation of surface oxygens followed by transformation of oxide layer to metal surface covered by hydroxyls. This appears to be consistent with experiments⁵² where it was shown that the oxidized Ir(110) surface exhibits hydrogen adsorption/desorption in contrast to Ir(111). Adsorption of O* atop of Ir atoms becomes favorable only at very high potentials (above $1.2 V_{\text{RHE}}$).

To simulate the oxidized Ir(100) surface we adopt a structural model suggested by Seriani et al. for Pt(100).⁶⁰ We may assume that oxidation of Ir(100) proceeds through adsorption of oxygen followed by initial formation of an ultrathin IrO-like layer due to the shift of every second row of Ir atoms to obtain the square-planar coordination of Ir with four oxygens. This configuration is found to be more stable than a layer of chemisorbed oxygen atoms and becomes thermodynamically favorable at about $0.4 V_{\text{RHE}}$ (the bold blue line in Figure 7). Below $0.4 V_{\text{RHE}}$ the oxide layer on Ir(100)

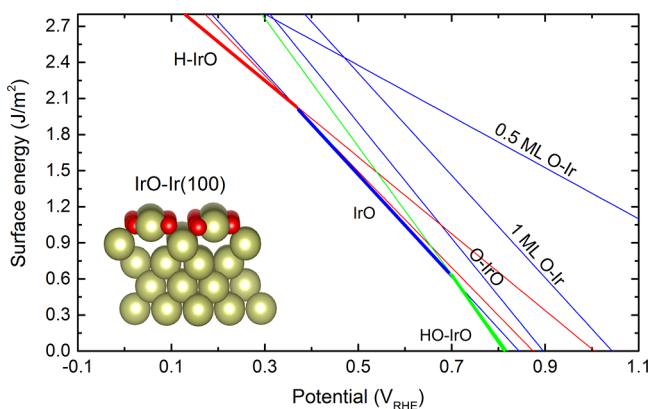
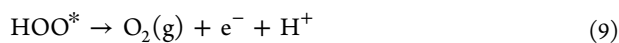
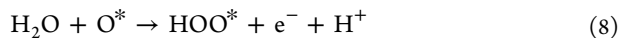
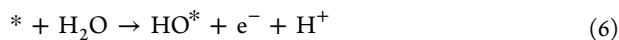


Figure 7. Surface energy as a function of potential and O/OH/H coverage on the IrO–Ir(100) surface. Bold lines define the most stable configuration under considered potential. Red, green and blue lines correspond to various H, OH and O coverages, respectively. Lines for the Ir metal surface are presented as a reference. The inset represents a structural model of the oxide precursor on the Ir(100) surface.

also shows a good propensity for hydrogen adsorption on top of Ir atoms, whereas the formation of the hydroxyl monolayer becomes favorable at potentials higher than $0.7 V_{\text{RHE}}$.

In general, the oxide precursors on all three Ir surfaces are found to be considerably more stable than the corresponding metal surfaces covered with a monolayer of oxygen at the same potentials. In electrochemical environment they could be covered with low amounts of hydroxyls or oxygen atoms, while a strong oxidation of oxide precursor surface leads to the structural transformations followed by bulk oxide growth or metal dissolution.

Catalytic Activity of the Ir Oxide Precursors toward OER. Since thin films of Ir oxide formed on Ir electrocatalysts were shown to play an important role in enhancing OER, in this section we investigate catalytic activity of Ir–O precursors toward OER to understand why their activity for OER may differ from metallic Ir and IrO₂. Conventionally, OER on metal-based electrocatalysts is assumed to proceed through the water nuclear attack (WNA) mechanism^{18,61} described by the following sequence of four electrochemical steps:



Our calculations reveal a very low activity toward OER of metallic Ir(100), Ir(110), and Ir(111) covered with a single monolayer of bridging oxygen atoms where water nuclear attack to form OOH* (step 3) on the surface turns out to be the potential-determining step of the overall OER (Figure 8). These results are in full agreement with previous theoretical calculations for RuO₂⁶² indicating that doubly coordinated oxygen atoms of RuO₂(110) are inactive toward OER. For the same reason we find that an oxide precursor formed on Ir(111) is inert toward OER. We suggest that OER in these cases could be coupled with dissolution and surface restructuring (e.g., through buckling on the IrO₂–Ir(111) precursor) that could lower OER thermodynamic overpotentials. Here, we focus on

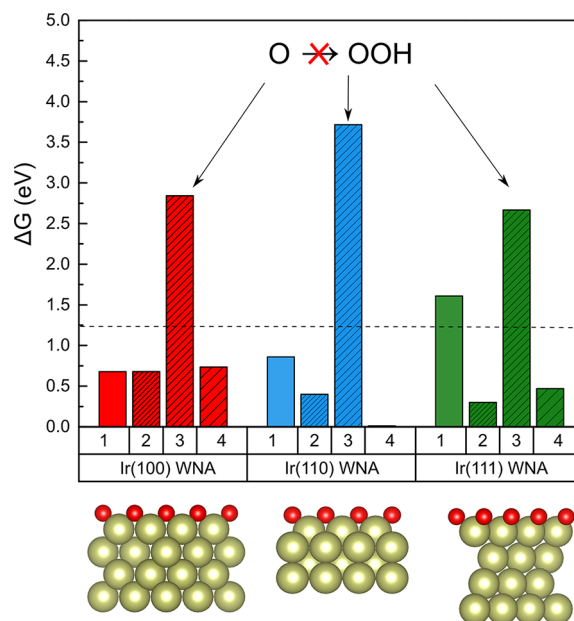
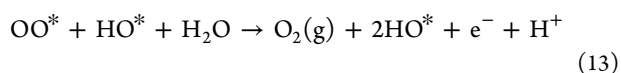
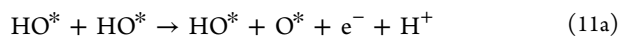
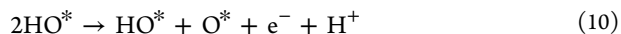


Figure 8. Gibbs free energy steps corresponding to the OER intermediates at the oxidized Ir(100), Ir(110), and Ir(111) surfaces.

the catalytic activity of oxide precursors formed on the Ir(110) and Ir(100) surfaces.

Since we find that a high coverage of O/OH adsorbates on oxide precursors can lead to significant structural transformations, we analyze OER when only two adjacent sites of the precursor are occupied by OH groups. In contrast to the oxidized metal surfaces (Figure 8), thermodynamic overpotentials for oxide precursors become considerably lower for WNA mechanism and the IrO₂–Ir(110) precursor elicits lower thermodynamic overpotentials than the rutile IrO₂(110) surface (see Figure 9). Moreover, in the case of IrO–Ir(100) we find that the two neighboring oxygens on the surface tend to form a dimer due to a favorable interatomic distance which could facilitate OER via an alternative reaction mechanism that includes the interaction of two adjacent M–O units (M = Ir) (I2M mechanism):



In this case the Gibbs energy loss for the potential-determining step of OER at IrO–Ir(100) becomes significantly lower than it is found for the WNA mechanism on the same Ir surface and at rutile IrO₂(110). At the IrO₂–Ir(110) surface the I2M mechanism is also possible since dimerization of the two adjacent oxygens (reaction 11) is energetically favorable, however, the thermodynamic overpotential for reaction 12 is estimated to be larger than the one for the WNA mechanism. We note that the I2M mechanism becomes energetically favorable for the corresponding oxide precursors due to short distances between adjacent metallic sites being 2.74 and 2.48 Å for IrO₂–Ir(110) and IrO–Ir(100), respectively, whereas for

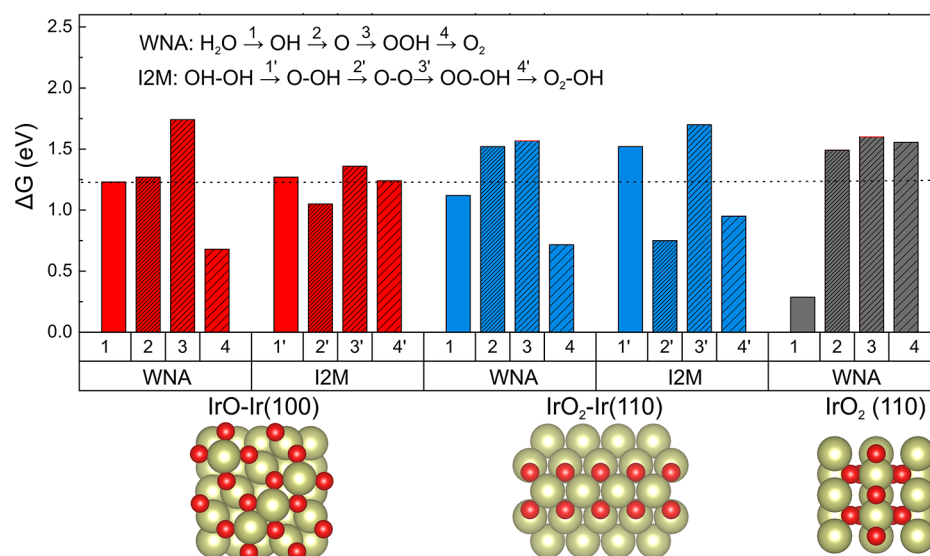


Figure 9. Gibbs free energy steps corresponding to the OER intermediates on the oxide precursors IrO-Ir(100) and IrO₂-Ir(110). Two four-step mechanisms (WNA and I2M) are analyzed. The horizontal dashed line at 1.23 V corresponds to the ideal OER catalyst for which all four steps would be equal to 1.23 V assuming zero thermodynamic overpotential.

IrO₂(110) the distance between the two active sites is considerably larger (3.18 Å). The possibility of the I2M mechanism on Ir was previously discussed⁶³ where it was experimentally demonstrated using marked oxygen atoms that some O₂ is formed exclusively from oxygen atoms belonging to the oxidized Ir surface. Recent DFT calculations also revealed that the I2M mechanism is energetically preferable for Ir molecular complexes attached to Ir-oxide surface.⁶⁴

Our simulations indeed demonstrate that oxide precursors should play an important role in thermodynamics of OER by lowering the reaction thermodynamic overpotential, in agreement with experimental data on the catalytic activity for nonstoichiometric oxides at Ir surfaces.¹⁶ However, the question of how stability and OER activity of metal catalysts are coupled dynamically including surface restructuring and the role of dissolution/deposition intermediates deserves a separate detailed study.

CONCLUSIONS

In this study, *ab initio* thermodynamics in conjunction with computational hydrogen electrode approach was employed to examine thermodynamic stability and catalytic activity of iridium surfaces in an electrochemical environment. All considered single-crystal Ir surfaces favor hydrogen adsorption at low electrode potentials, followed by a region of coadsorbed hydroxyl and water species and then oxidized metallic surfaces at high potentials that eventually transform into thermodynamically stable IrO₂. It was found that the most energetically stable (111) facet of Ir is characterized by coadsorption of H and OH species, whereas for Pt(111) H and OH adsorption regions are separated by a wide double layer region. Overall, Ir surfaces display weaker (stronger) binding of hydrogen (oxygen) than Pt being more oxophilic which is consistent with a higher susceptibility of Ir for oxidation. The computed surface energies enable prediction of equilibrium Ir nanoparticle shapes as a function of electrode potential. In particular, the fraction of the Ir(111) surface, dominant under ultrahigh vacuum conditions, is significantly decreased at high potentials, while the strong binding of O* species on

Ir(110) at potentials above 0.7 V_{RHE} results in a higher ratio of Ir(110) sites.

Although we have not examined the kinetics of the formation of oxide precursors on Ir, by using the atomic structures of Ir-O thin films formed on Ir from the literature we also analyzed their thermodynamic stability under electrochemical conditions. Specifically, we showed that these precursors are covered with OH and O at intermediate potentials, while further oxidation leads to structural transformations that could initiate either bulk-like oxide growth or metal dissolution. We also revealed that these Ir oxide thin layers should be responsible for enhanced catalytic activity toward OER with the prevailing I2M mechanism for the Ir(100)-IrO system.

AUTHOR INFORMATION

Corresponding Author

*(V.A.) E-mail: valexandrov2@unl.edu. Telephone: +1 402 4725323.

ORCID

Konstantin Klyukin: [0000-0001-8325-8725](https://orcid.org/0000-0001-8325-8725)

Vitaly Alexandrov: [0000-0003-2063-6914](https://orcid.org/0000-0003-2063-6914)

Notes

The authors declare no competing financial interest.

ACKNOWLEDGMENTS

This research used resources of the National Energy Research Scientific Computing Center (NERSC), a U.S. Department of Energy Office of Science User Facility operated under Contract No. DE-AC02-05CH11231. This research has been partially supported by the donors of the Petroleum Research Fund, administered by the American Chemical Society (ACS PRF 58410-DNIS).

REFERENCES

- (1) Cherevko, S.; Geiger, S.; Kasian, O.; Mingers, A.; Mayrhofer, K. J. Oxygen evolution activity and stability of iridium in acidic media. Part 1.—Metallic iridium. *J. Electroanal. Chem.* **2016**, *773*, 69–78.

- (2) Pfeifer, V.; Jones, T. E.; Wrabetz, S.; Massué, C.; Velasco Vélez, J. J.; Arrigo, R.; Scherzer, M.; Piccinin, S.; Hävecker, M.; Knop-Gericke, A.; et al. Reactive oxygen species in iridium-based OER catalysts. *Chemical science* **2016**, *7*, 6791–6795.
- (3) Strmcnik, D.; Uchimura, M.; Wang, C.; Subbaraman, R.; Danilovic, N.; Van Der Vliet, D.; Paulikas, A. P.; Stamenkovic, V. R.; Markovic, N. M. Improving the hydrogen oxidation reaction rate by promotion of hydroxyl adsorption. *Nat. Chem.* **2013**, *5*, 300.
- (4) Durst, J.; Simon, C.; Hasché, F.; Gasteiger, H. A. Hydrogen oxidation and evolution reaction kinetics on carbon supported Pt, Ir, Rh, and Pd electrocatalysts in acidic media. *J. Electrochem. Soc.* **2015**, *162*, F190–F203.
- (5) Cho, Y.-B.; Yu, A.; Lee, C.; Kim, M. H.; Lee, Y. Fundamental Study of Facile and Stable Hydrogen Evolution Reaction at Electrospun Ir and Ru Mixed Oxide Nanofibers. *ACS Appl. Mater. Interfaces* **2018**, *10*, 541–549.
- (6) Zhdanov, V. On the kinetics of CO oxidation over the Ir (111) surface. *Surf. Sci.* **1984**, *137*, 515–526.
- (7) Lopes, P. P.; Strmcnik, D.; Jirkovsky, J. S.; Connell, J. G.; Stamenkovic, V.; Markovic, N. Double layer effects in electrocatalysis: The oxygen reduction reaction and ethanol oxidation reaction on Au (111), Pt (111) and Ir (111) in alkaline media containing Na and Li cations. *Catal. Today* **2016**, *262*, 41–47.
- (8) Reier, T.; Oezaslan, M.; Strasser, P. Electrocatalytic oxygen evolution reaction (OER) on Ru, Ir, and Pt catalysts: a comparative study of nanoparticles and bulk materials. *ACS Catal.* **2012**, *2*, 1765–1772.
- (9) McCrory, C. C.; Jung, S.; Peters, J. C.; Jaramillo, T. F. Benchmarking heterogeneous electrocatalysts for the oxygen evolution reaction. *J. Am. Chem. Soc.* **2013**, *135*, 16977–16987.
- (10) Kasian, O.; Grote, J.-P.; Geiger, S.; Cherevko, S.; Mayrhofer, K. J. The common intermediates of oxygen evolution and dissolution reactions during water electrolysis on iridium. *Angew. Chem., Int. Ed.* **2018**, *57*, 2488–2491.
- (11) Kötz, R.; Stucki, S.; Scherson, D.; Kolb, D. In-situ identification of RuO₄ as the corrosion product during oxygen evolution on ruthenium in acid media. *J. Electroanal. Chem. Interfacial Electrochem.* **1984**, *172*, 211–219.
- (12) Chang, S. H.; Connell, J. G.; Danilovic, N.; Subbaraman, R.; Chang, K.-C.; Stamenkovic, V. R.; Markovic, N. M. Activity–stability relationship in the surface electrochemistry of the oxygen evolution reaction. *Faraday Discuss.* **2014**, *176*, 125–133.
- (13) Roy, C.; Rao, R. R.; Stoerzinger, K. A.; Hwang, J.; Rossmeisl, J.; Chorkendorff, I.; Shao-Horn, Y.; Stephens, I. E. Trends in Activity and Dissolution on RuO₂ under Oxygen Evolution Conditions: Particles versus Well-Defined Extended Surfaces. *ACS Energy Letters* **2018**, *3*, 2045–2051.
- (14) Spoeeri, C.; Kwan, J. T. H.; Bonakdarpour, A.; Wilkinson, D. P.; Strasser, P. The stability challenges of oxygen evolving catalysts: Towards a common fundamental understanding and mitigation of catalyst degradation. *Angew. Chem., Int. Ed.* **2017**, *56*, 5994–6021.
- (15) Barnard, A. Modelling of nanoparticles: approaches to morphology and evolution. *Rep. Prog. Phys.* **2010**, *73*, 086502.
- (16) Li, T.; Kasian, O.; Cherevko, S.; Zhang, S.; Geiger, S.; Scheu, C.; Felfer, P.; Raabe, D.; Gault, B.; Mayrhofer, K. J. Atomic-scale insights into surface species of electrocatalysts in three dimensions. *Nature Catalysis* **2018**, *1*, 300.
- (17) Jovanovic, P.; Hodnik, N.; Ruiz-Zepeda, F.; Arcon, I.; Jozinovic, B.; Zorko, M.; Bele, M.; Sala, M.; Selih, V. S.; Hocevar, S.; et al. Electrochemical dissolution of iridium and iridium oxide particles in acidic media: transmission electron microscopy, electrochemical flow cell coupled to inductively coupled plasma mass spectrometry, and X-ray absorption spectroscopy study. *J. Am. Chem. Soc.* **2017**, *139*, 12837–12846.
- (18) Reier, T.; Nong, H. N.; Teschner, D.; Schlögl, R.; Strasser, P. Electrocatalytic oxygen evolution reaction in acidic environments—reaction mechanisms and catalysts. *Adv. Energy Mater.* **2017**, *7*, 1601275.
- (19) Arroyo-Curras, N.; Bard, A. J. Iridium oxidation as observed by surface interrogation scanning electrochemical microscopy. *J. Phys. Chem. C* **2015**, *119*, 8147–8154.
- (20) Zhang, H.; Soon, A.; Delley, B.; Stampfl, C. Stability, structure, and electronic properties of chemisorbed oxygen and thin surface oxides on Ir (111). *Phys. Rev. B: Condens. Matter Mater. Phys.* **2008**, *78*, 045436.
- (21) Kaghazchi, P.; Jacob, T. First-principles studies on clean and oxygen-adsorbed Ir (110) surfaces. *Phys. Rev. B: Condens. Matter Mater. Phys.* **2007**, *76*, 245425.
- (22) Ferstl, P.; Schmitt, T.; Schneider, M.; Hammer, L.; Michl, A.; Müller, S. Structure and ordering of oxygen on unreconstructed Ir (100). *Phys. Rev. B: Condens. Matter Mater. Phys.* **2016**, *93*, 235406.
- (23) Perdew, J. P.; Burke, K.; Ernzerhof, M. Generalized gradient approximation made simple. *Phys. Rev. Lett.* **1996**, *77*, 3865.
- (24) Kresse, G.; Furthmüller, J. Efficiency of ab-initio total energy calculations for metals and semiconductors using a plane-wave basis set. *Comput. Mater. Sci.* **1996**, *6*, 15–50.
- (25) Kresse, G.; Furthmüller, J. Efficient iterative schemes for ab initio total-energy calculations using a plane-wave basis set. *Phys. Rev. B: Condens. Matter Mater. Phys.* **1996**, *54*, 11169.
- (26) Grimme, S.; Antony, J.; Ehrlich, S.; Krieg, H. A consistent and accurate ab initio parametrization of density functional dispersion correction (DFT-D) for the 94 elements H-Pu. *J. Chem. Phys.* **2010**, *132*, 154104.
- (27) Grimme, S.; Ehrlich, S.; Goerigk, L. Effect of the damping function in dispersion corrected density functional theory. *J. Comput. Chem.* **2011**, *32*, 1456–1465.
- (28) Bengtsson, L. Dipole correction for surface supercell calculations. *Phys. Rev. B: Condens. Matter Mater. Phys.* **1999**, *59*, 12301.
- (29) Exner, K. S.; Anton, J.; Jacob, T.; Over, H. Microscopic Insights into the Chlorine Evolution Reaction on RuO₂ (110): a Mechanistic Ab Initio Atomistic Thermodynamics Study. *Electrocatalysis* **2015**, *6*, 163–172.
- (30) Exner, K. S.; Over, H. Kinetics of Electrocatalytic Reactions from First-Principles: A Critical Comparison with the Ab Initio Thermodynamics Approach. *Acc. Chem. Res.* **2017**, *50*, 1240–1247.
- (31) McCrum, I. T.; Janik, M. J. pH and alkali cation effects on the Pt cyclic voltammogram explained using density functional theory. *J. Phys. Chem. C* **2016**, *120*, 457–471.
- (32) Nørskov, J. K.; Rossmeisl, J.; Logadottir, A.; Lindqvist, L.; Kitchin, J. R.; Bligaard, T.; Jonsson, H. Origin of the overpotential for oxygen reduction at a fuel-cell cathode. *J. Phys. Chem. B* **2004**, *108*, 17886–17892.
- (33) Zucker, R. V.; Chatain, D.; Dahmen, U.; Hagège, S.; Carter, W. C. New software tools for the calculation and display of isolated and attached interfacial-energy minimizing particle shapes. *J. Mater. Sci.* **2012**, *47*, 8290–8302.
- (34) McCrum, I. T.; Chen, X.; Schwarz, K. A.; Janik, M. J.; Koper, M. T. Effect of Step Density and Orientation on the Apparent pH Dependence of Hydrogen and Hydroxide Adsorption on Stepped Platinum Surfaces. *J. Phys. Chem. C* **2018**, *122*, 16756–16764.
- (35) Anderson, A. B. Insights into electrocatalysis. *Phys. Chem. Chem. Phys.* **2012**, *14*, 1330–1338.
- (36) Rossmeisl, J.; Qu, Z.-W.; Zhu, H.; Kroes, G.-J.; Nørskov, J. K. Electrolysis of water on oxide surfaces. *J. Electroanal. Chem.* **2007**, *607*, 83–89.
- (37) Man, I. C.; Su, H.-Y.; Calle-Vallejo, F.; Hansen, H. A.; Martínez, J. I.; Inoglu, N. G.; Kitchin, J.; Jaramillo, T. F.; Nørskov, J. K.; Rossmeisl, J. Universality in oxygen evolution electrocatalysis on oxide surfaces. *ChemCatChem* **2011**, *3*, 1159–1165.
- (38) Briquet, L. G.; Sarwar, M.; Mugo, J.; Jones, G.; Calle-Vallejo, F. A new type of scaling relations to assess the accuracy of computational predictions of catalytic activities applied to the oxygen evolution reaction. *ChemCatChem* **2017**, *9*, 1261–1268.
- (39) Gauthier, J. A.; Dickens, C. F.; Chen, L. D.; Doyle, A. D.; Nørskov, J. K. Solvation Effects for Oxygen Evolution Reaction Catalysis on IrO₂(110). *J. Phys. Chem. C* **2017**, *121*, 11455–11463.

- (40) Karlberg, G. Adsorption trends for water, hydroxyl, oxygen, and hydrogen on transition-metal and platinum-skin surfaces. *Phys. Rev. B: Condens. Matter Mater. Phys.* **2006**, *74*, 153414.
- (41) Hagedorn, C. J.; Weiss, M. J.; Weinberg, W. H. Dissociative chemisorption of hydrogen on Ir (111): Evidence for terminal site adsorption. *Phys. Rev. B: Condens. Matter Mater. Phys.* **1999**, *60*, R14016.
- (42) Hanh, T. T. T.; Takimoto, Y.; Sugino, O. First-principles thermodynamic description of hydrogen electroadsorption on the Pt (111) surface. *Surf. Sci.* **2014**, *625*, 104–111.
- (43) Arman, M. A.; Klein, A.; Ferstl, P.; Valookaran, A.; Gustafson, J.; Schulte, K.; Lundgren, E.; Heinz, K.; Schneider, A.; Mittendorfer, F.; et al. Adsorption of hydrogen on stable and metastable Ir (100) surfaces. *Surf. Sci.* **2017**, *656*, 66–76.
- (44) McCrum, I. T.; Hickner, M. A.; Janik, M. J. First-Principles Calculation of Pt Surface Energies in an Electrochemical Environment: Thermodynamic Driving Forces for Surface Faceting and Nanoparticle Reconstruction. *Langmuir* **2017**, *33*, 7043–7052.
- (45) Lew, W.; Crowe, M. C.; Campbell, C. T.; Carrasco, J.; Michaelides, A. The energy of hydroxyl coadsorbed with water on Pt (111). *J. Phys. Chem. C* **2011**, *115*, 23008–23012.
- (46) Motoo, S.; Furuya, N. Effect of anions on hydrogen and oxygen adsorption on iridium single crystal surfaces. *J. Electroanal. Chem. Interfacial Electrochem.* **1984**, *181*, 301–305.
- (47) Wan, L.-J.; Hara, M.; Inukai, J.; Itaya, K. In situ scanning tunneling microscopy of well-defined Ir (111) surface: high-resolution imaging of adsorbed sulfate. *J. Phys. Chem. B* **1999**, *103*, 6978–6983.
- (48) Pajkossy, T.; Kibler, L.; Kolb, D. Voltammetry and impedance measurements of Ir(111) electrodes in aqueous solutions. *J. Electroanal. Chem.* **2005**, *582*, 69–75.
- (49) Ganassin, A.; Sebastián, P.; Climent, V.; Schuhmann, W.; Bandarenka, A. S.; Feliu, J. On the pH Dependence of the Potential of Maximum Entropy of Ir (111) Electrodes. *Sci. Rep.* **2017**, *7*, 1246.
- (50) Pekoz, R.; Worner, S.; Ghiringhelli, L. M.; Donadio, D. Trends in the adsorption and dissociation of water clusters on flat and stepped metallic surfaces. *J. Phys. Chem. C* **2014**, *118*, 29990–29998.
- (51) Sheng, W.; Myint, M.; Chen, J. G.; Yan, Y. Correlating the hydrogen evolution reaction activity in alkaline electrolytes with the hydrogen binding energy on monometallic surfaces. *Energy Environ. Sci.* **2013**, *6*, 1509–1512.
- (52) Özer, E.; Spöri, C.; Reier, T.; Strasser, P. Iridium (111), Iridium (110), and Ruthenium (0001) Single Crystals as Model Catalysts for the Oxygen Evolution Reaction: Insights into the Electrochemical Oxide Formation and Electrocatalytic Activity. *ChemCatChem* **2017**, *9*, 597–603.
- (53) Furuya, N.; Koide, S. Hydrogen adsorption on iridium single-crystal surfaces. *Surf. Sci.* **1990**, *226*, 221–225.
- (54) Kurnikov, B.; Zhurin, A.; Chernyi, V.; Vasil'ev, Y. Adsorption of oxygen on a smooth iridium electrode. *Electrokhimiya* **1973**, *9*, 833–836.
- (55) Bryl, R.; Olewicz, T.; Visart de Bocarmé, T.; Kruse, N. Thermal Faceting of Clean and Oxygen-Covered Ir Nanocrystals. *J. Phys. Chem. C* **2011**, *115*, 2761–2768.
- (56) Kaghazchi, P.; Jacob, T.; Ermanoski, I.; Chen, W.; Madey, T. E. First-principles studies on oxygen-induced faceting of Ir (210). *ACS Nano* **2008**, *2*, 1280–1288.
- (57) He, Y.; Stierle, A.; Li, W.; Farkas, A.; Kasper, N.; Over, H. Oxidation of Ir (111): From O-Ir-O Trilayer to Bulk Oxide Formation. *J. Phys. Chem. C* **2008**, *112*, 11946–11953.
- (58) Eslamibidgoli, M. J.; Eikerling, M. H. Atomistic Mechanism of Pt Extraction at Oxidized Surfaces: Insights from DFT. *Electrocatalysis* **2016**, *7*, 345–354.
- (59) Pedersen, T. M.; Li, W. X.; Hammer, B. Structure and activity of oxidized Pt (110) and α -PtO₂. *Phys. Chem. Chem. Phys.* **2006**, *8*, 1566–1574.
- (60) Seriani, N.; Pompe, W.; Ciacchi, L. C. Catalytic oxidation activity of Pt₃O₄ surfaces and thin films. *J. Phys. Chem. B* **2006**, *110*, 14860–14869.
- (61) Suen, N.-T.; Hung, S.-F.; Quan, Q.; Zhang, N.; Xu, Y.-J.; Chen, H. M. Electrocatalysis for the oxygen evolution reaction: recent development and future perspectives. *Chem. Soc. Rev.* **2017**, *46*, 337–365.
- (62) Dickens, C. F.; Nørskov, J. K. A theoretical investigation into the role of surface defects for oxygen evolution on RuO₂. *J. Phys. Chem. C* **2017**, *121*, 18516–18524.
- (63) Fierro, S.; Nagel, T.; Baltruschat, H.; Comminellis, C. Investigation of the oxygen evolution reaction on Ti/IrO₂ electrodes using isotope labelling and on-line mass spectrometry. *Electrochem. Commun.* **2007**, *9*, 1969–1974.
- (64) García-Melchor, M.; Vilella, L.; López, N.; Vojvodic, A. Computationally Probing the Performance of Hybrid, Heterogeneous, and Homogeneous Iridium-Based Catalysts for Water Oxidation. *ChemCatChem* **2016**, *8*, 1792–1798.